

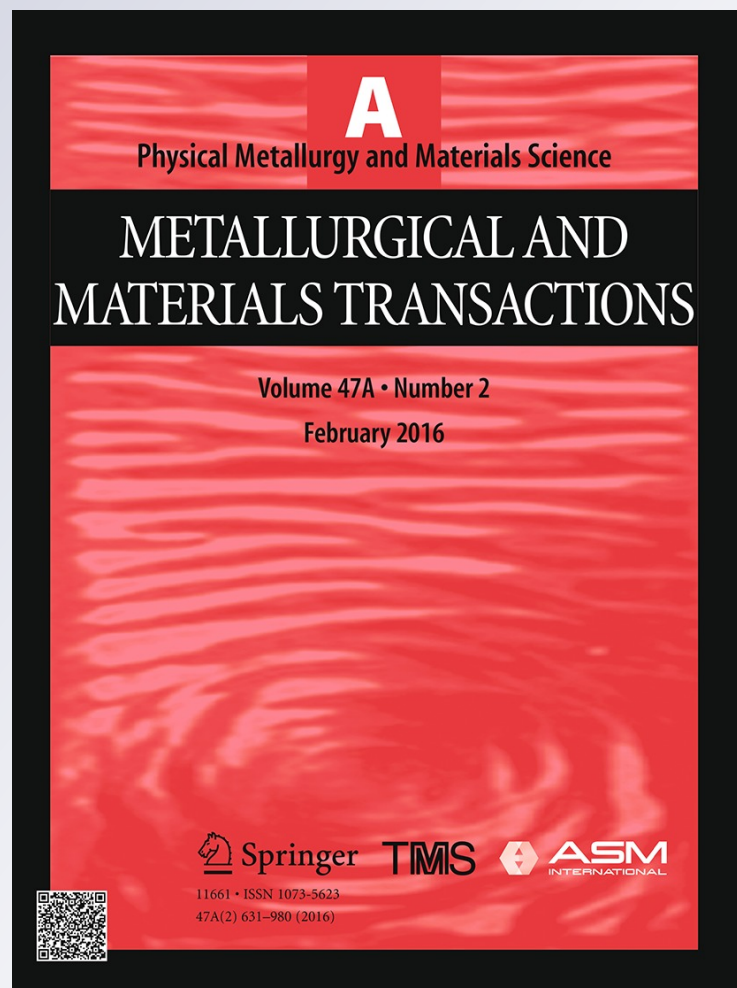
In Situ Measurement and Prediction of Stresses and Strains During Casting of Steel

Daniel Galles & Christoph Beckermann

**Metallurgical and Materials
Transactions A**

ISSN 1073-5623
Volume 47
Number 2

Metall and Mat Trans A (2016)
47:811-829
DOI 10.1007/s11661-015-3184-x



Your article is protected by copyright and all rights are held exclusively by The Minerals, Metals & Materials Society and ASM International. This e-offprint is for personal use only and shall not be self-archived in electronic repositories. If you wish to self-archive your article, please use the accepted manuscript version for posting on your own website. You may further deposit the accepted manuscript version in any repository, provided it is only made publicly available 12 months after official publication or later and provided acknowledgement is given to the original source of publication and a link is inserted to the published article on Springer's website. The link must be accompanied by the following text: "The final publication is available at link.springer.com".

In Situ Measurement and Prediction of Stresses and Strains During Casting of Steel



DANIEL GALLES and CHRISTOPH BECKERMANN

Modeling the thermo-mechanical behavior of steel during casting is of great importance for the prediction of distortions and cracks. In this study, an elasto-visco-plastic constitutive law is calibrated with mechanical measurements from casting experiments. A steel bar is solidified in a sand mold and strained by applying a force to bolts that are embedded in the two ends of the bar. The temporal evolutions of the restraint force and the bar's length change are measured *in situ*. The experiments are simulated by inputting calculated transient temperature fields into a finite element stress analysis that employs the measured forces as boundary conditions. The thermal strain predictions are validated using data from experiments without a restraint. Initial estimates of the constitutive model parameters are obtained from available mechanical test data involving reheated steel specimens. The temperature dependence of the strain rate sensitivity exponent is then adjusted until the measured and predicted length changes of the strained bars agree. The resulting calibrated mechanical property dataset is valid for the high-temperature austenite phase of steel. The data reveal a significantly different mechanical behavior during casting compared to what the stress-strain data from reheated specimens show.

DOI: 10.1007/s11661-015-3184-x

© The Minerals, Metals & Materials Society and ASM International 2015

I. INTRODUCTION

DURING casting of steel, mechanically and thermally induced stresses are the source of several problems that continue to plague industry. Mechanically induced stresses are created when the steel contacts another part of the casting system (*e.g.*, a core in shape casting, the mold or rolls in a continuous casting machine), while thermally induced stresses are created by uneven cooling. The stresses generate distortions, which in turn lead to dimensional inaccuracies and defects in the as-cast product. For example, if distortions occur near the end of solidification, hot tears may form, which necessitate the casting to be scrapped. In continuous casting processes, the strand must be carefully cooled to avoid cracking. In shape casting, distortions can lead to a lengthy trial-and-error process of modifying pattern allowances to meet dimensional requirements. Hence, the ability to accurately predict stresses for steel casting can lead to more efficient processes and higher quality cast products.

The complexities associated with a casting process (*i.e.*, multi-physics constitutive laws, thermo-mechanical coupling, three-dimensional geometries) provide considerable challenges to efficient and accurate stress modeling. In recent years, however, computational advancements have spurred the development of complex casting deformation models to better predict stresses

and strains in steel castings. For such modeling, realistic mechanical properties of the steel are needed for the elasto-visco-plastic constitutive law used in a stress analysis. These temperature dependent mechanical properties are normally determined using high-temperature stress-strain data acquired from either tensile^[1-3] or creep^[4] tests that are performed using reheated steel specimens. Wray^[3] comprehensively characterized the mechanical behavior of austenite throughout a range of temperatures [1123 K to 1523 K (850 °C to 1250 °C)], carbon contents (0.005 to 1.54 pct), and strain rates (6×10^{-6} to 2×10^{-2} 1/s). Suzuki *et al.*^[4] performed a series of creep tests on austenite at different stress levels (4.1 to 9.8 MPa) from 1523 K to 1673 K (1250 °C to 1400 °C); the results of the tests were fitted to a time hardening equation.

Such tests have provided the crucial data needed to develop constitutive laws for stress modeling in steel castings.^[5,6] Anand^[5] used the measurements of Wray^[2] to determine the parameters of a viscoplastic model for the austenite phase of low-carbon steel. Utilizing the data of Wray^[3] and Suzuki *et al.*,^[4] Kozłowski *et al.*^[6] developed four constitutive relations to model the time dependent deformation behavior of austenite; Model III was found to be the best compromise, based on its ability to fit the test data, reasonable behavior under complex loading conditions, and numerical stability. This model was subsequently used in numerous studies by Thomas and coworkers^[7-12] and Fachinotti and coworkers.^[13,14] Although each investigation focused on a specific topic (*i.e.*, model comparison,^[10,13] computational performance,^[8,11,14] *etc.*), the common goal of all of the studies was the prediction of stresses and strains during steel continuous casting processes.

DANIEL GALLES, Graduate Research Assistant, and CHRISTOPH BECKERMANN, Professor, are with the Department of Mechanical and Industrial Engineering, University of Iowa, Iowa City, IA 52242. Contact e-mail: becker@engineering.uiowa.edu

Manuscript submitted February 10, 2015.

Article published online November 16, 2015

The above investigations represent significant advancements in stress modeling of steel casting processes. Model accuracy was predicated on the assumption that the mechanical test data from reheated steel specimens sufficiently characterizes the thermo-mechanical behavior during a casting process. However, the microstructure of the steel specimens can be expected to evolve significantly during the reheating and isothermal holding periods of the mechanical tests, which in turn can affect the mechanical properties. This is especially true for the relatively long holding times typical of creep tests. In addition, Zhang *et al.*^[15] showed the existence of significant thermal gradients within mechanical test specimens, leading to heterogeneous deformations. For these reasons, the development of constitutive data from mechanical testing with reheated specimens may not be suitable for stress modeling of steel casting. Consequently, the following researchers studied the mechanical behavior of steel during casting through *in situ* testing.

Parkins and Cowan^[16] produced steel bars with flanges on either end, which constrained the bar from free contraction and induced distortions. The contraction of the bar was continuously measured using dial gauges; however, no restraint forces were measured. Monroe and Beckermann^[17] continuously measured the contraction and restraint force in a T-shaped steel casting to study hot tears. Ackermann *et al.*^[18] developed the submerged split-chill tensile test (SSCT) to characterize the mechanical behavior of steel during solidification for predicting hot tears. While this experiment gives valuable insight into the formation of hot tears, it is not particularly useful for the modeling of casting deformations; the complex geometry of the apparatus introduces uncertainty as to which force and displacements are being measured. Rowen *et al.*^[19] modeled the submerged split-chill compression (SSCC) test, which is a simplified version of the SSCT test. To validate the model, the simulated and measured forces were matched during solidification. However, because no displacements are measured in the SSCC test, the accuracy of the model parameters could not be verified.

In the present work, a mechanical constitutive model for steel casting is developed using *in situ* force and displacement measurements. The experiments involve a rectangular bar that is strained during casting to induce stresses in the bar. The temporal evolutions of the restraint force and the bar's axial length change are measured *in situ* with load bolts and linear variable differential transformers (LVDTs), respectively. Additional casting trials are performed without any restraint to measure the thermal strains (*i.e.*, free shrink). The stresses and strains during the casting experiments are predicted using a general-purpose finite element stress analysis code. A one-way temperature–displacement coupling is adopted; transient temperature fields are calculated with casting simulation software and subsequently used as input for the finite element simulations. The experiments without the restraint are simulated first to ensure accurate modeling of the thermal expansion behavior of the steel. Then, using the measured forces as a boundary condition, the experiments with the restraint

are simulated. Initially, the model parameters for the elasto–visco–plastic constitutive law are estimated with stress–strain data from mechanical tests using reheated specimens. Through a trial-and-error process, any disagreements between measured and predicted length changes of the strained bars are eliminated through adjustments to a single viscoplastic parameter, until good agreement is obtained. Through these modifications, a mechanical constitutive model for steel is calibrated using *in situ* data from a casting process.

II. DESCRIPTION OF EXPERIMENTS

A. Experimental Setup

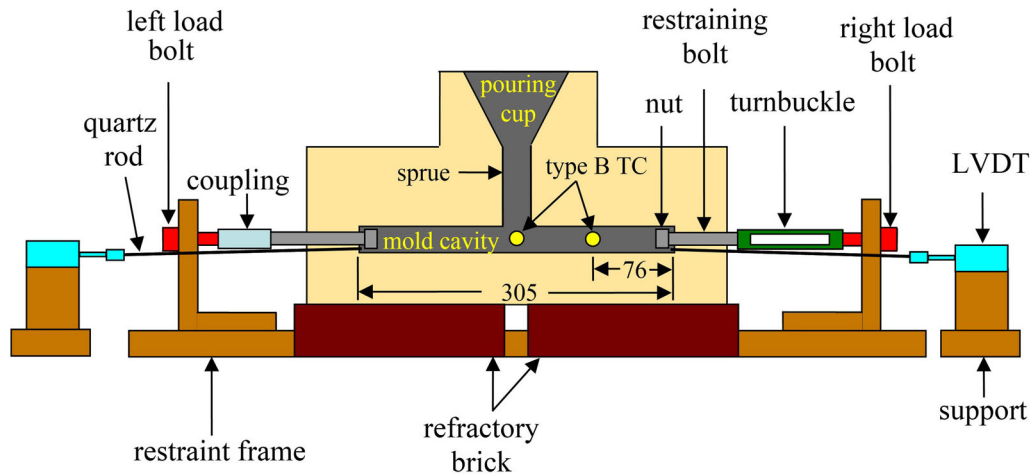
The experimental design was motivated from the presumption that the total strain, ϵ_{total} , can be decomposed into the sum of its mechanical, ϵ_{mech} , and thermal, ϵ_{th} , parts, as

$$\epsilon_{\text{total}} = \epsilon_{\text{mech}} + \epsilon_{\text{th}}. \quad [1]$$

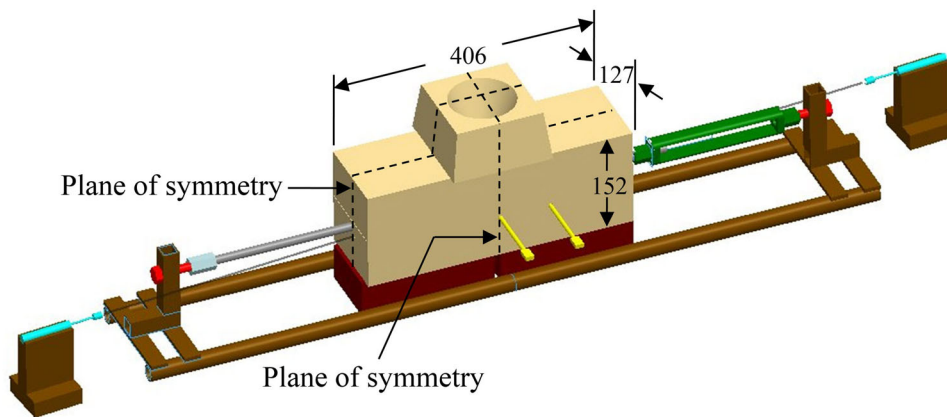
Consequently, two sets of casting trials, referred to as “strained” and “unrestrained,” were designed to measure ϵ_{total} and ϵ_{th} independently. Schematics of the setup for the strained bar experiments are shown in Figure 1. A slender steel bar (305 mm long with a 25 mm square cross section) was cast in a sand mold. The mold cavity was filled through the pouring cup and sprue (which also serves to feed the casting) located at the center of the bar. With the aid of a restraint frame and steel bolts inserted at the two ends of the bar, the thermal shrinkage along the axis of the bar was constrained during solidification and cooling to induce stresses. Preliminary experiments showed that this effect alone did not generate sufficient viscoplastic strains. Therefore, a turnbuckle was added in line with one of the restraining bolts to produce additional distortions. In order to prevent slippage between the casting and the bolts, nuts were inserted over the ends of the bolts in the mold cavity. Removal of the restraint, restraining bolts, load bolts, coupling, turnbuckle, and nuts reduces the schematic in Figure 1 to the setup for the unrestrained bar experiments.

Contact interactions at the mold–metal interface were minimized due to the simple geometry and the symmetry of the setup about the two vertical planes shown in Figure 1(b). Friction forces between the casting and mold generated negligible mechanical strains due to the small casting weight. For these reasons, dimensional changes in the unrestrained bars were due to thermal strains only, whereas all measured distortions in the strained bars were a consequence of the restraint.

In order to collect data, several devices were used; a load bolt was connected in line with each restraining bolt (*via* a coupling on the left side and turnbuckle on the right side of Figure 1(a)) to continuously measure the axial restraint force at both ends of the bar. The axial displacements at each end of the bar were transmitted *via* quartz rods to LVDTs, from which the axial length change was calculated by adding the LVDT



(a) Mid-section cut



(b) CAD Drawing

Fig. 1—Schematics of the setup for the strained bar experiments. All dimensions are in mm. Forces, displacements, and temperatures were measured *in situ* with load bolts, LVDTs, and type B thermocouples, respectively.

measurements together. Finally, type B thermocouples were encased in quartz tubes and inserted into the mold cavity to measure steel temperatures directly under the sprue and 76 mm from the end of the casting.

To build the molds, silica lake sand was bonded using a phenolic urethane no-bake (PUNB) binder system (which accounted for 1.25 pct of the total mold weight) and mixed with a 55:45 ratio of Part 1 (PEP SET[®] 1000) to Part 2 (PEP SET[®] 2000). The chemical reaction was accelerated with a catalyst (PEP SET[®] 3501) based on 6 pct of the binder weight.

B. Casting Procedure

Experiments were performed at the University of Northern Iowa's Metal Casting Center. The target chemistry was ASTM A216 grade WCB carbon steel, which was prepared in an induction furnace and poured from a 250 lb heat at approximately 1873 K (1600 °C). The measured compositions of the cast steel for each experiment are provided in Table I. Following pouring, the strained bars were allowed to partially solidify, after









which the turnbuckle was engaged (*i.e.*, turned) to lengthen the bar and induce distortions. Due to differences in casting chemistry, the solidification times varied among the casting heats. A value of 1673 K (1400 °C) (the approximate temperature at the end of solidification) was typically assumed as the temperature at which the casting could transmit stresses. Once the thermocouple reading (under the sprue) had fallen below this temperature, the turnbuckle was slowly engaged for a period of 30 to 60 seconds.

C. Experimental Results

A total of eight casting experiments, 5 strained and 3 unrestrained, were performed. In order to identify individual bars, a numbering system was adopted (*e.g.*, strained 1, unrestrained 1). In addition, a unique color was assigned to each bar in order to distinguish between curves on all result plots. These identifiers are also provided in Table I.

Since type B thermocouples lose their accuracy at room temperature, data were acquired until the castings

Table I. Summary of the Color Codes (Used in the Plots) and Casting Chemistries for all Unrestrained (unr.) and Strained (str.) Bars. Iron (Fe) Constitutes the Remaining Balance of the Chemistry Compositions

Set	Color Code	Casting Chemistry								
		Pct C	Pct Si	Pct Mn	Pct P	Pct S	Pct Cr	Pct Al	Pct Cu	Pct Fe
unr. 1		0.21	0.50	0.52	0.072	0.002	0.08	0.070	0.08	bal.
unr. 2		0.32	0.69	0.64	0.025	0.014	0.23	0.054	0.10	bal.
unr. 3		0.25	0.59	0.55	0.012	0.014	0.04	0.069	0.04	bal.
str. 1		0.25	0.58	0.62	0.022	0.016	0.03	0.087	0.05	bal.
str. 2		0.42	0.78	0.65	0.068	0.010	0.09	0.057	0.08	bal.
str. 3		0.25	0.61	0.56	0.021	0.017	0.10	0.071	0.08	bal.
str. 4		0.25	0.45	0.46	0.019	0.017	0.04	0.045	0.03	bal.
str. 5		0.30	0.57	0.41	0.031	0.026	0.02	0.056	0.01	bal.

cooled to approximately 373 K (100 °C). The time range (12000 seconds) needed to record the results down to this temperature is henceforth referred to as the complete time scale. Several important features occurring at early times are difficult to see on this scale. Therefore, intermediate and initial time scales (showing the initial 1000 and 250 seconds, respectively) are also utilized to present the experimental results.

The measured axial length changes, plotted as a function of time, are shown for all experiments in Figure 2. For the unrestrained bar experiments, excellent reproducibility of the measurements can be seen, as the three curves essentially lie on top of each other. Starting from the initial time ($t = 0$ second), the unrestrained axial length decreases (as a result of thermal contractions) until approximately 500 seconds. At this time, a volumetric expansion (due to the solid-state phase transformation from austenite to pearlite and α -ferrite) occurred and is manifested as a positive slope beginning at 600 seconds. Because the bar temperatures varied spatially, this transformation commenced at different times throughout the casting. As a result, the axial length increases over an expanded period of approximately 300 seconds, after which it decreases monotonically until room temperature.

For the strained bar experiments, the restraint force impacted the axial length change substantially (see Figure 2). Initially, the axial lengths decreased similarly to those of the unrestrained bar experiments. However, shortly after the restraint force was applied, the strained bars elongated, which can be seen in Figure 2(c) as a positive slope for all strained curves. During this time, the strained and unrestrained curves diverge, as considerable viscoplastic strains were generated. The straining periods (*i.e.*, the period during which the turnbuckle was engaged) for all strained bar experiments are represented in Figure 2(c) by double-headed arrows bounded by vertical dashed lines. Note that the onset of straining and the straining period varied among the 5 strained bar experiments. This was done on purpose in order to achieve different temperature ranges for the deformations. In other words, the five strained bar experiments were not intended to duplicate each other. At the end of the straining period, the axial length change remained

constant for a brief period before continuing to decrease, as thermal strains dominated. At some point during cooling, the steel gained sufficient strength, after which yielding no longer occurred; at all ensuing times, the measured axial length changes for the strained bar experiments were due to thermal strains only. This can be clearly observed in Figure 2(a); after 1500 seconds, the strained and unrestrained bars contracted at the same rate (*i.e.*, strained and unrestrained curves are parallel), which implies the presence of thermal strains only. Hence, for the experiments in which the quartz probes failed at late times (strained 2, 3, and 4), the displacements could be reconstructed (shown as dashed lines) with confidence using data from other experiments (either strained or unrestrained).

The measured restraint forces for the strained bar experiments are plotted as a function of time on the primary vertical axis in Figures 3(a) through (c). In addition, the nominal stresses (defined as the restraint force divided by the nominal cross-sectional area of the bar) are plotted on the secondary axis. At some time during the initial 200 seconds, engagement of the turnbuckle rapidly increased the restraint force (nominal stress) to roughly 3 kN (5 MPa). From the initial time scale in Figure 3(c), the straining period (shown as a double-headed arrow) for each experiment is determined as the time span from when the force begins to increase until a local maximum is reached. The decrease immediately following this peak is due to stress relaxation resulting from creep effects. After this brief decrease, the ensuing thermal contractions acted to increase the restraint force, albeit at a slower rate. Once again, the effect of the solid-state phase transformation can be seen beginning at approximately 600 seconds, as volumetric expansion of the bar caused a relaxation in the restraint, resulting in a slight decrease of the restraint forces. Upon completion of this transformation, the forces continued to slowly increase up to 12,000 seconds.

A comparison between the forces measured at either end of the casting revealed a difference. An example for one of the experiments (strained bar 4) is shown in Figure 3(d); the “left” and “right” curves refer to the location of the load bolts in Figure 1(a). The figure clearly shows that the left force is larger than the right force. The

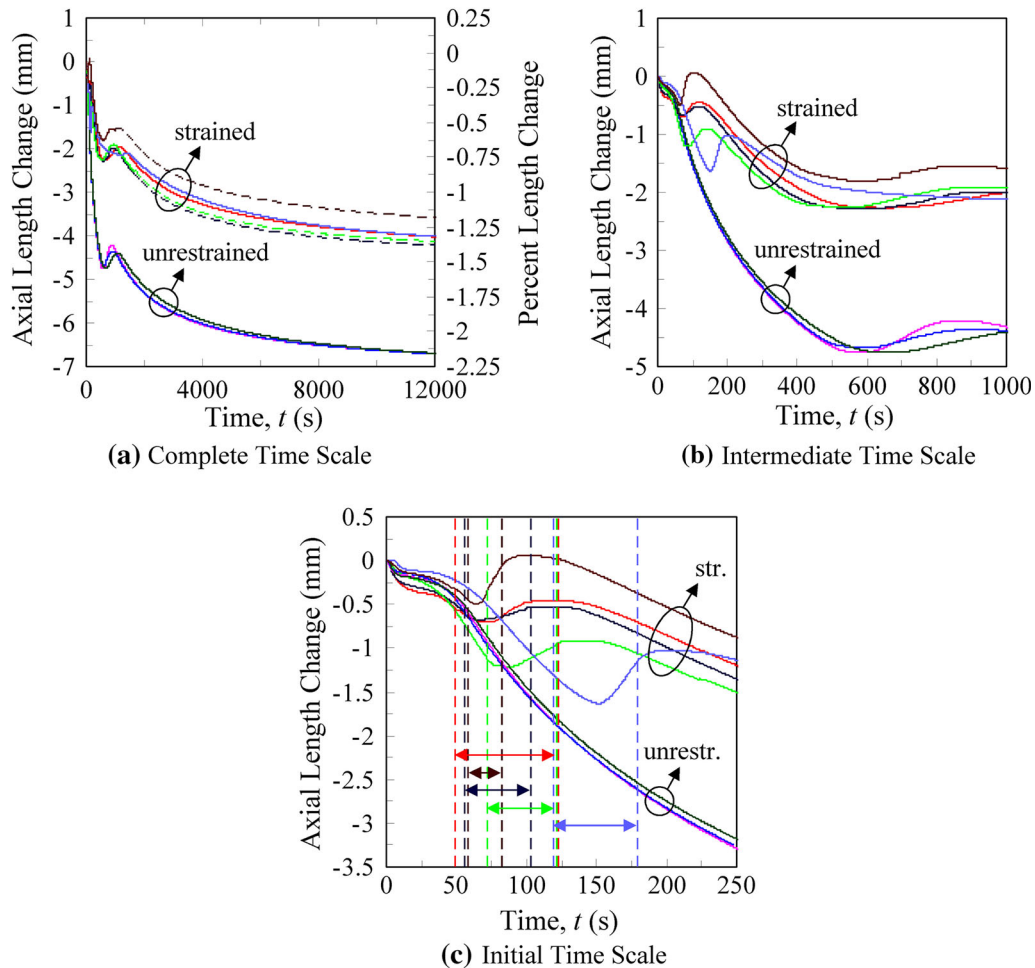


Fig. 2—Measured axial length change for the strained and unrestrained bar experiments plotted on complete (a), intermediate (b), and initial (c) time scales. The double-headed arrows that are bounded by vertical dashed lines of the same color in (c) represent the straining periods.

difference increases throughout the straining period to reach a value of approximately 1 MPa after 100 seconds. This difference (roughly 20 pct) is due to a sprue–mold interaction and will be accounted for by an additional boundary condition in the finite element simulations.

The strained bar 5 sprue diameter (1.5 inches) was larger than the other sprue diameters (1 inch). As a result, several differences can be seen on the displacement and force plots; due to a larger hot spot (directly under the sprue), a longer waiting period was required before engaging the turnbuckle to ensure that the casting had reached coherency and could transmit stresses. This can be seen in Figure 3(c); the restraint force began increasing after 120 seconds, whereas the buildup of the other forces commenced earlier (between 50 and 75 seconds). Accordingly, elongation of the bar also occurred later, as shown in Figure 2(c). Additionally, the larger sprue created larger temperature gradients along the axial direction of the bar. Therefore, the solid-state phase transformation for the entire bar (which is manifested as a “wiggle” in the displacement curves) occurred over a longer period for strained bar 5 than the other bars, as seen in Figure 2(a).

An example of measured temperatures for one of the experiments (strained bar 5) is shown in Figures 4(a) and

(b). Due to space limitations, the thermocouple measurements for all experiments cannot be presented here. Taking a discrete time derivative of the measured temperatures, the cooling rate plot of Figure 4(c) is obtained. The liquidus temperature (T_{liq}), which represents the onset of solidification and latent heat release, is given by the initial local minimum in the cooling rate curve. As can be seen from Figure 4(c), the cooling rate increases with decreasing temperature, which can be attributed to a decreasing rate of latent heat release during solidification. The cooling rate reaches a local maximum when solidification is complete. The corresponding temperature is termed here, for simplicity, the solidus temperature (T_{sol}). Note that due to variations in the steel chemistry (see Table I), the measured liquidus and solidus temperatures were different in each experiment.

III. THERMAL SIMULATIONS AND THERMOPHYSICAL PROPERTIES

Temperatures were predicted using the commercial casting simulation software MAGMASOFT[®],^[20] which required several inputs. Mold properties were taken directly from the MAGMASOFT[®] database.

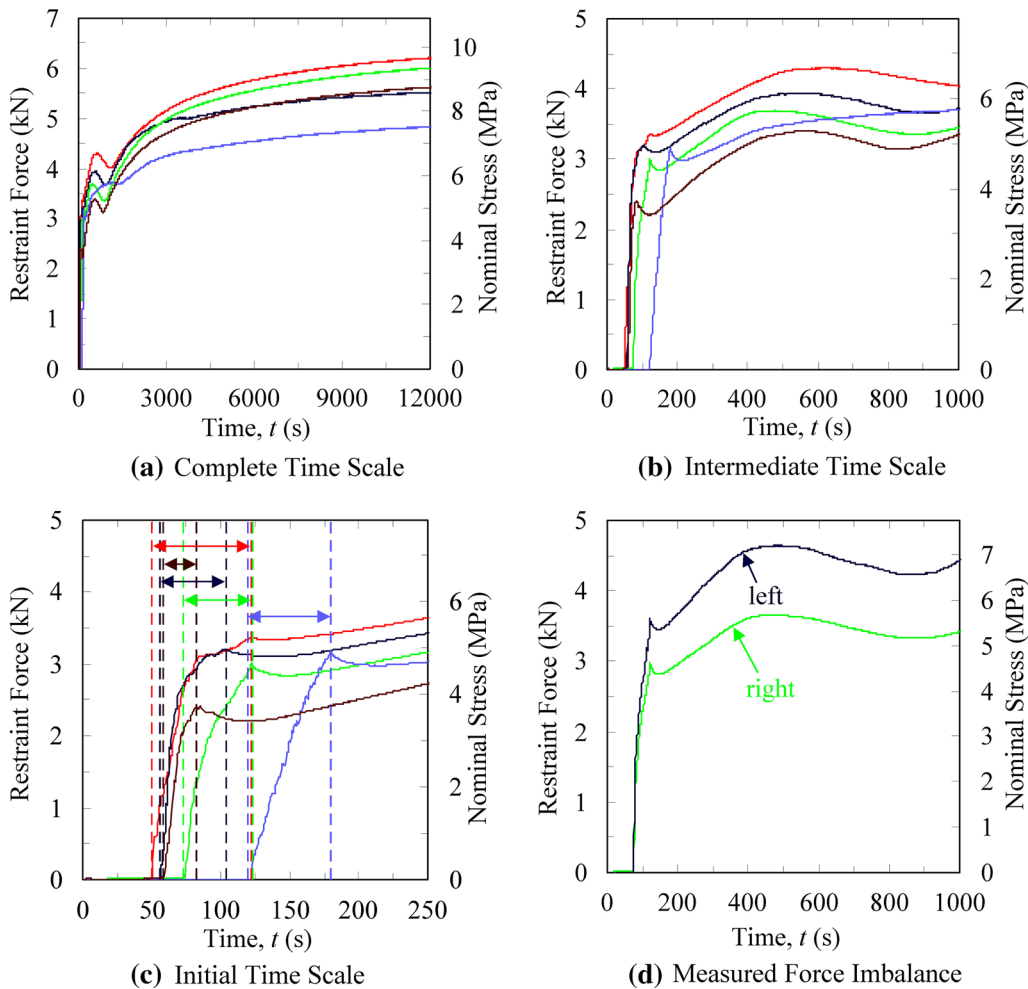


Fig. 3—Measured restraint force for the strained bar experiments plotted on complete (a), intermediate (b), and initial (c) time scales. The double-headed arrows that are bounded by vertical dashed lines of the same color in (c) represent the straining periods. A measured force imbalance (d) (strained bar 4 shown) was observed between the “right” and “left” load bolts [locations shown in Fig. 1(a)] for all strained experiments.

Temperature dependent thermophysical properties (*i.e.*, density, specific heat, thermal conductivity) of the steel, as well as the solid volume fraction as a function of temperature and the latent heat of solidification, were calculated with IDS^[21] software using the measured steel chemistries for each experiment (Table I). The interfacial heat transfer coefficient (at the mold–metal interface) was initially specified as a constant value.

In general, using the initial property datasets and boundary conditions did not result in good agreement between measured and predicted temperatures. Therefore, through a trial-and-error process, several adjustments to the simulation inputs were made. The process is described in detail elsewhere.^[22,23] The main modifications involved the temperature dependent interfacial heat transfer coefficient and solid fraction. In particular, the solid fraction curve was adjusted to exactly match the measured liquidus and solidus temperatures and measured cooling rates during the solidification interval. An example of an adjusted solid fraction curve is provided in Figure 4(d). The slight kink in the solid fraction curve at about $g_s = 0.3$ is due to the transformation of δ -ferrite to austenite. As is typical for cast steels, the total

solidification interval exceeds 120 K ($-153\text{ }^\circ\text{C}$), but more than 90 pct of the liquid solidifies within the first 50 K. It is important to note that a different solid fraction curve resulted from the thermal simulation for each of the eight experiments. These variations can be attributed to the different steel compositions (see Table I). After the adjustments, excellent agreement was achieved between measured and predicted temperatures for each experiment. An example of this agreement (from the strained bar 5 simulation) is shown in Figures 4(a, overall time scale) and (b, intermediate time scale).

An example of predicted temperature fields (from the strained bar 1 simulation) at the beginning and end of the straining period is shown in Figures 5(a) and (b), respectively. At any location in the bar, large temperature drops [$\delta T > 175\text{ K}$ ($-98\text{ }^\circ\text{C}$)] can be observed between the beginning and end of the straining period. In addition, significant temperature variations can be seen both over the length of the bar and over each of the cross sections, labeled A–D. Section A is located directly under the sprue and contains the highest temperatures in the bar at any particular time, whereas section D is near the end of the bar and contains lower temperatures.

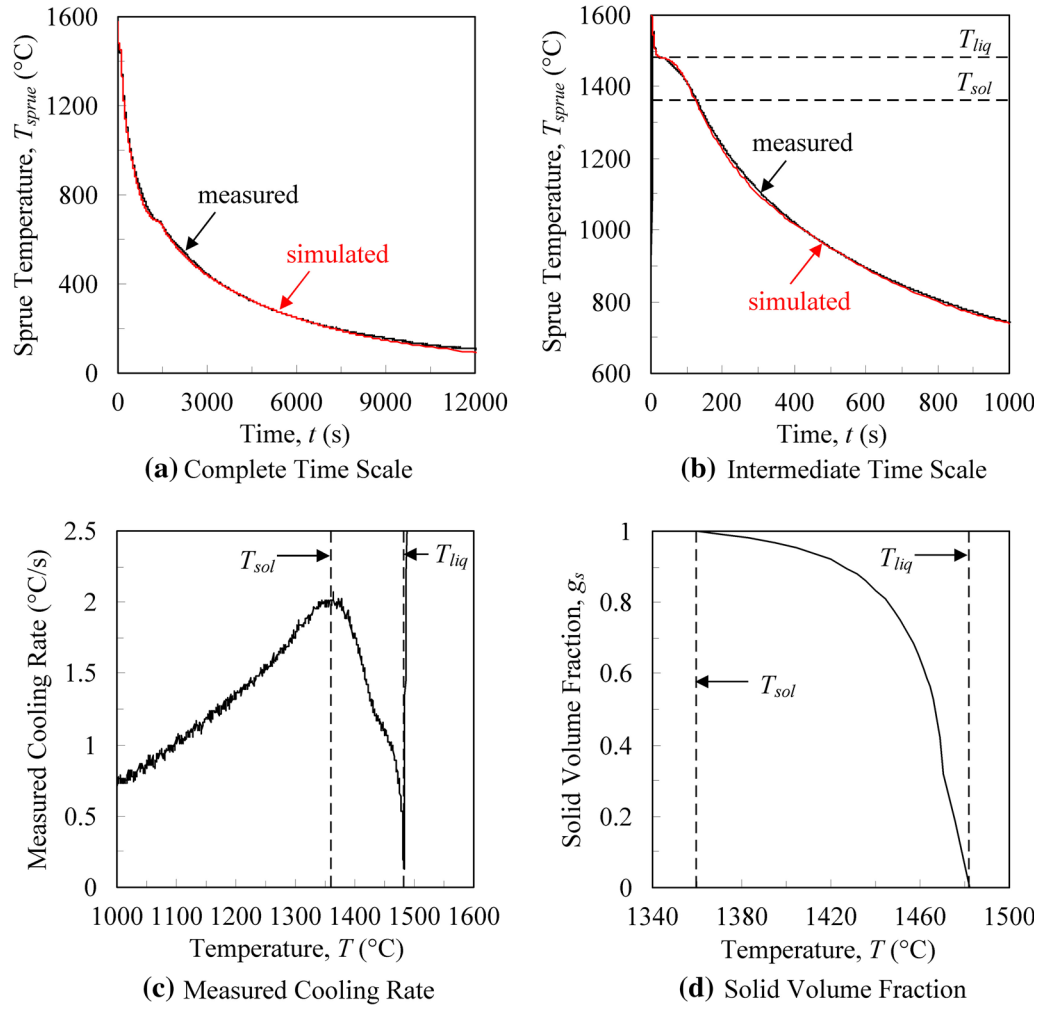


Fig. 4—Comparison (from strained bar 5) between measured and predicted sprue temperatures on complete (a) and intermediate (b) time scales. The solidus and liquidus temperatures are determined from the measured cooling curve in (c). The adjusted solid volume fraction curve used for the simulations is shown in (d).

For the stress model used in this study, the strains are dependent on the solid fraction, g_s (see the following section). Due to the hot spot created by the sprue at the bar's mid-length, cross section A (see Figure 5) is the last to solidify. The predicted solid fractions for cross section A at the onset of straining are shown for all strained bars in Figure 5(c). The values vary from $g_s \approx 0.6$ at the middle of strained bar 1 to $g_s = 1$ at all locations in strained bar 4. In most of the experiments, however, the bar was close to or fully solidified when straining commenced. Hence, the effect of the solid fraction in the stress model can be expected to be small. Nonetheless, the variations from bar to bar emphasize again that the five strained bar experiments provide mechanical data for different temperature ranges and are not intended to duplicate each other. The predicted temperature fields in the steel for each experiment were saved at a large number of time steps (approximately 100) and subsequently mapped onto the finite element mesh used in the stress analysis (see below).

IV. STRESS MODEL AND PROPERTIES

A. Stress Model

The stress model is adopted from Monroe and coworkers.^[24,25] In this model, the effective stress depends on the solid fraction. This dependency eliminates the need to model each region in a casting (*i.e.*, fully liquid, semi-solid, fully solid) as a separate material and therefore leads to a robust model capable of predicting the strains and stresses over the entire temperature range using a single constitutive relation. For $g_s = 1$ (fully solid), the model reduces to a standard elasto-visco-plastic model.

Assuming negligible inertial effects, body forces, and momentum transport between the solid and liquid during solidification, the solid momentum equation is given by

$$\nabla \cdot \tilde{\sigma} = 0, \quad [2]$$

where $\tilde{\sigma}$ is the effective stress tensor. The semi-solid mush created during solidification is treated as a com-

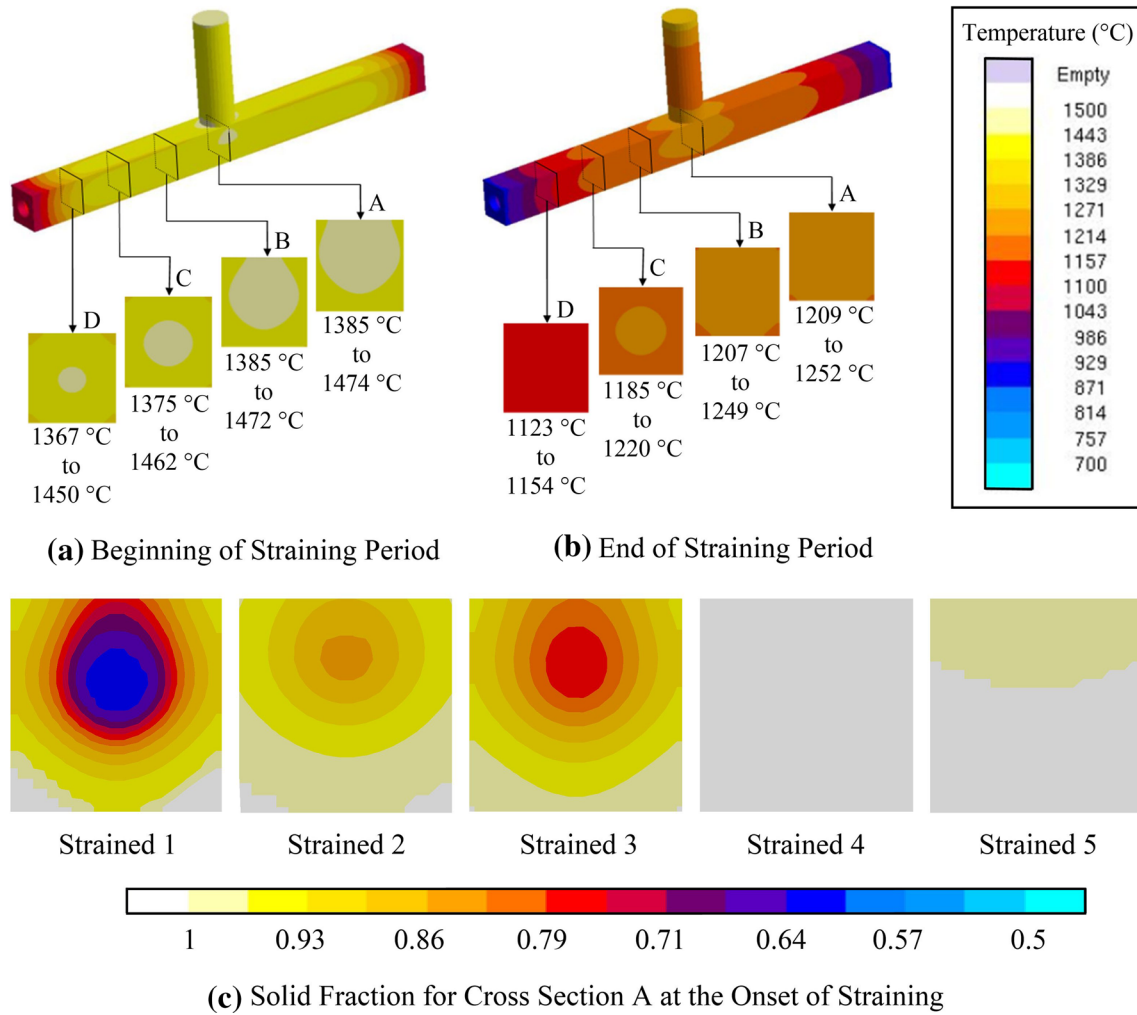


Fig. 5—Predicted temperature fields for strained bar 1 at the beginning (a) and end (b) of the straining period. The predicted solid fraction contours for cross section A [location shown in (a) and (b)] at the onset of straining.

pressible porous medium where the stress depends on the pressure. In such media, the stress tensor is given by Reference 26

$$\tilde{\sigma} = g_s \sigma_s + g_s p_l \mathbf{I}, \quad [3]$$

where g_s is the solid volume fraction, σ_s is the Cauchy stress tensor of the solid material, and \mathbf{I} is the second-order identity tensor. Near the end of solidification, the liquid pressure minimally contributes to casting stresses and is set to $p_l = 0$.

Using small strain theory, the strain tensor, ϵ , is decomposed into the elastic (ϵ_e), thermal (ϵ_{th}), and viscoplastic (ϵ_{vp}) components as

$$\epsilon = \epsilon_e + \epsilon_{th} + \epsilon_{vp}. \quad [4]$$

The elastic strain is determined from Hooke's law as

$$\tilde{\sigma} = \mathbf{C}_e : \epsilon_e, \quad [5]$$

where \mathbf{C}_e is the elastic stiffness tensor. Assuming a homogeneous and isotropic material, it is given by

$$\mathbf{C}_e = \frac{E}{3(1-2\nu)} \mathbf{I} \otimes \frac{E}{3(1+\nu)} \mathbf{I}_{dev}, \quad [6]$$

where E is the effective Young's modulus, ν is the effective Poisson's ratio, \mathbf{I} is the fourth-order identity tensor, and \mathbf{I}_{dev} is the fourth-order deviatoric identity tensor. The effective elastic properties are determined using the following solid fraction dependent relations^[27]:

$$E = E_s \left(\frac{g_s - g_s^{coh}}{1 - g_s^{coh}} \right)^{n^E} \quad [7]$$

and

$$\nu = \nu_0 + \left(\frac{g_s - g_s^{coh}}{1 - g_s^{coh}} \right) (\nu_s - \nu_0). \quad [8]$$

In Eq. [7], the effective Young's modulus is scaled between Young's modulus of the solid material, E_s , at $g_s = 1$ and a negligibly small value at the coherency

solid fraction, g_s^{coh} . The coherency solid fraction refers to the moment during solidification when the solid dendrites become sufficiently entangled to form a continuous network that allows stresses to be transmitted. The coherency solid fraction was taken as $g_s^{\text{coh}} = 0.5$ and the power coefficient, n^E , as 2.5.^[28] Eq. [8] shows that the effective Poisson's ratio is linearly scaled from the fully solid value at $g_s = 1$ to a minimum Poisson's ratio, $\nu_0 = 0.14$ ^[27] at g_s^{coh} .

The thermal strain is given by

$$\boldsymbol{\varepsilon}_{\text{th}} = \alpha_{\text{tot}}(T - T_{\text{th}})\mathbf{I}, \quad [9]$$

where T_{th} is the temperature at the onset of thermal contraction. Additionally, α_{tot} is the total linear thermal expansion coefficient and defined as

$$\alpha_{\text{tot}} = \frac{1}{(T - T_{\text{th}})} \int_{T_{\text{th}}}^T -\frac{1}{3\rho_s} \frac{d\rho_s}{dT} dT, \quad [10]$$

where ρ_s is the solid density. Eq. [10] is the form of the linear thermal expansion coefficient required by ABAQUS[®].^[29]

The viscoplastic strain rate is given by an associated flow law^[30]:

$$\dot{\boldsymbol{\varepsilon}}_{\text{vp}} = \dot{\gamma} \frac{\partial \sigma_{\text{eq}}}{\partial \boldsymbol{\sigma}}, \quad [11]$$

where $\dot{\gamma}$ is the scalar flow parameter and σ_{eq} is the equivalent stress. The latter is taken as^[31]

$$\sigma_{\text{eq}}^2 = A_1 q_s^2 + A_2 p_s^2. \quad [12]$$

In Eq. [12], the pressure of the solid, $p_s = -1/3(\tilde{\boldsymbol{\sigma}} : \mathbf{I})$, is the mean of the normal stresses from the effective stress tensor. The von Mises stress of the solid, $q_s = \sqrt{3/2(\boldsymbol{\tau}_s : \boldsymbol{\tau}_s)}$, is determined from the deviatoric stress tensor, $\boldsymbol{\tau}_s = \boldsymbol{\sigma} + p_s \mathbf{I}$. The equivalent stress can be thought of as the scalar form of the effective stress tensor. The functions A_1 and A_2 are from Cocks model^[32] and defined as

$$A_1 = \left(1 + \frac{2}{3}(1 - g_s^*)\right) (g_s^*)^{-2/(1+m)} \quad [13]$$

and

$$A_2 = \frac{9}{4} \left(\frac{1 - g_s^*}{2 - g_s^*}\right) \left(\frac{2}{1 + m}\right) (g_s^*)^{-2/(1+m)}, \quad [14]$$

where m is the strain rate sensitivity exponent and g_s^* is the scaled solid fraction. In the limit where the solid fraction is unity, the equivalent stress reduces to the von Mises stress, where A_1 is equal to unity and A_2 is equal to zero. The scaled solid fraction is defined as

$$g_s^* = \left(\frac{g_s - g_s^{\text{coh}}}{g_s^{\text{coal}} - g_s^{\text{coh}}}\right), \quad [15]$$

where g_s^{coal} is the coalescence solid fraction, which occurs near the end of solidification and represents the upper limit of the scaled solid fraction, above which scaling is not employed. The coalescence solid fraction was set to 0.85, the value from a previous study^[33] below which ductile fracture occurred in a round tensile bar due to coalescence of voids. For the present study, the bar was near complete solidification when straining began (see Figure 5(c)), with only the interior region under the sprue containing semi-solid material in some experiments. Therefore, the coherency and coalescence solid fractions had a negligibly small effect on the present results.

The dynamic yield stress, σ_{dy} , defines the stress-strain relationship after yielding occurs. The relation used here is taken from Marin and McDowell^[34] and given by

$$\sigma_{\text{dy}} = \sigma_0 \left(1 + \frac{\varepsilon_{\text{eq}}}{\varepsilon_0}\right)^n \left(1 + \frac{\dot{\varepsilon}_{\text{eq}}}{\dot{\varepsilon}_0}\right)^m, \quad [16]$$

where σ_0 is the initial yield stress, n is the strain hardening exponent, and m is the strain rate sensitivity exponent. The equivalent plastic strain rate, $\dot{\varepsilon}_{\text{eq}}$, is determined from the scalar dissipation of energy according to

$$\dot{\varepsilon}_{\text{eq}} = \frac{\tilde{\boldsymbol{\sigma}} : \dot{\boldsymbol{\varepsilon}}_{\text{vp}}}{g_s \sigma_{\text{dy}}}. \quad [17]$$

The equivalent plastic strain, ε_{eq} , is obtained by integrating the equivalent plastic strain rate over time for temperatures below the annealing temperature. The annealing temperature is taken as T_{sol} . Additionally, ε_0 is the reference strain, defined as $\varepsilon_0 = \sigma_0 n / E$, and $\dot{\varepsilon}_0$ is the reference strain rate. The latter is given by the Arrhenius equation $\dot{\varepsilon}_0 = A \exp(-Q/RT)$, where A is the Arrhenius prefactor, Q is the activation energy, R is the universal gas constant, and T is the absolute temperature. When the equivalent stress exceeds the dynamic yield stress, the equivalent plastic strain is increased to satisfy $\sigma_{\text{eq}} = \sigma_{\text{dy}}$. Combining this relation with Eq. [12] defines the yield surface as

$$f = \sigma_{\text{dy}}^2 - A_1 q_s^2 - A_2 p_s^2 = 0. \quad [18]$$

B. Mechanical Properties

The elastic properties were obtained from the literature. The temperature dependent Young's modulus was taken from Koric and Thomas.^[8] Also, because experimental observations of increased Poisson's ratio with temperature may be due to increasing amounts of creep during the test,^[35] a constant value of 0.3 was used.

Substituting the reference strain and reference strain rate definitions into the dynamic yield stress equation (Eq. [16]) gives

$$\sigma_{dy} = \sigma_0 \left(1 + \frac{E\epsilon_{eq}}{\sigma_0 n} \right)^n \left(1 + \frac{\dot{\epsilon}_{eq}}{A \exp(-Q/RT)} \right)^m. \quad [19]$$

Now it can be seen that 5 material parameters must be known: σ_0 , n , m , A , and Q . These parameters were estimated for austenite using data from the uniaxial tensile tests of Wray^[3] [1123 K (850 °C) $\leq T \leq$ 1523 K (1250 °C)] and Suzuki *et al.*^[4] [1523 K (1250 °C) $\leq T \leq$ 1673 K (1400 °C)] involving reheated steel specimens. The Levenberg–Marquardt algorithm, which minimizes the difference between measured and predicted values of a nonlinear function with a least squares method, was employed to perform the fit. Following the method of Kozłowski *et al.*,^[6] the initial yield stress (σ_0), strain hardening exponent (n), and strain rate sensitivity exponent (m) were initially estimated as quadratic functions of temperature but later reduced to linear, as differences between the fits were found to be small. The activation energy (Q) was estimated as a constant value. To account for carbon-content dependency, the Arrhenius prefactor (A) was estimated as a quadratic function of the carbon content.^[6] The estimated parameters are provided in Table II.

The estimated viscoplastic material parameters are plotted over the approximate temperature range of austenite [973 K (700 °C) $\leq T \leq$ 1773 K (1500 °C)] in Figure 6. Note, however, that the tensile test data are limited to a temperature range of 1123 K to 1523 K (850 °C to 1250 °C) for Wray^[3] and 1523 K to 1673 K (1250 °C to 1400 °C) for Suzuki *et al.*,^[4] which are denoted on all plots in Figure 6. Outside this range, the parameters were extrapolated. The δ -ferrite phase is present in the mushy zone at very high temperatures. However, for the carbon contents in this study (pct C > 0.2), δ -ferrite exists only at solid fractions below 0.5 at which the steel does not transmit stresses; therefore, the mechanical properties of δ -ferrite did not require consideration. The reference strain rate and reference strain (shown in Figures 6(c) and (d), respectively), were calculated from the expressions given below Eq. [17] and the values in Table II. The reference strain rate is shown for a representative carbon content of 0.25 pct (which is needed to calculate A); for the finite element simulations, the measured carbon content (shown in Table I) was used.

Figure 7 shows examples of the excellent agreement between measured and predicted stress–strain curves which is obtained using the present viscoplastic parameters. The comparisons are for a 0.29 pct carbon

content, two different temperatures [1223 K and 1373 K (950 °C and 1100 °C)], and a large range of strain rates. Similar agreement was obtained for all data in Wray^[3] and Suzuki *et al.*^[4]

Recall from the axial length change measurements (Figure 2) that the strained and unrestrained curves are essentially parallel after 1500 seconds (*i.e.*, after the solid-state phase transformation), and all strains at lower temperatures are purely thermal. Therefore, the stress model cannot be validated at temperatures below the austenite range using data from the present experiments, as no distortions occurred at temperatures below the solid-state phase transformation. For this reason, viscoplastic parameters were not estimated below 973 K (700 °C). Rather, the initial yield stress, σ_0 , was set to an arbitrarily high value in order to prevent the prediction of viscoplastic strains at lower temperatures.

V. STRESS SIMULATIONS

A. Procedure

The stress simulations were performed using the general-purpose finite element software ABAQUS[®]. The present constitutive model was implemented in a user-defined UMAT subroutine.^[36] To save computational costs, the simulation model was somewhat simplified. Frictional forces at the mold–metal interface were estimated to be negligibly small, and the mold was not included in the simulations. Additionally, the metal in the pouring cup did not contribute to distortions in the bars and was also excluded. Finally, the parts of the restraining bolts protruding from the casting (which only served to transmit forces) were omitted. The resulting ABAQUS[®] model for the strained bar is shown in Figure 8. Approximately 60,000 seconds-order tetrahedral elements (90,000 nodes) were used to generate the mesh.

For the strained bars, a zero displacement ($u_x = u_y = u_z = 0$) boundary condition was specified at one end of the bar. Although both ends translated during cooling, the axial length change is a relative displacement (between the bar ends); therefore, constraining one end was sufficient for the simulations. At the other end, the measured restraint force was assigned. In order to account for the force imbalance shown in Figure 3(c), the difference between the forces measured at the two ends was applied at the base of the sprue. Because the mold was excluded, an additional displacement boundary condition was required (shown on the right end of the model in Figure 8) to constrain the

Table II. Estimated Parameters from the Mechanical Tests of Wray^[3] and Suzuki *et al.*^[4]

Parameter	Expression	Units
Initial yield stress, σ_0	$5.729 \times 10^{-1} - 1.461 \times 10^{-4} T$	MPa
Strain hardening exponent, n	$2.457 \times 10^{-1} - 6.192 \times 10^{-5} T$	—
Strain rate sensitivity exponent, m	$4.924 \times 10^{-2} + 9.930 \times 10^{-5} T$	—
Arrhenius prefactor, A	$2.501 \times 10^4 + 1.246 \times 10^5 (\text{pct C}) + 1.240 \times 10^4 (\text{pct C})^2$	1/s
Activation energy, Q	354	kJ/mol

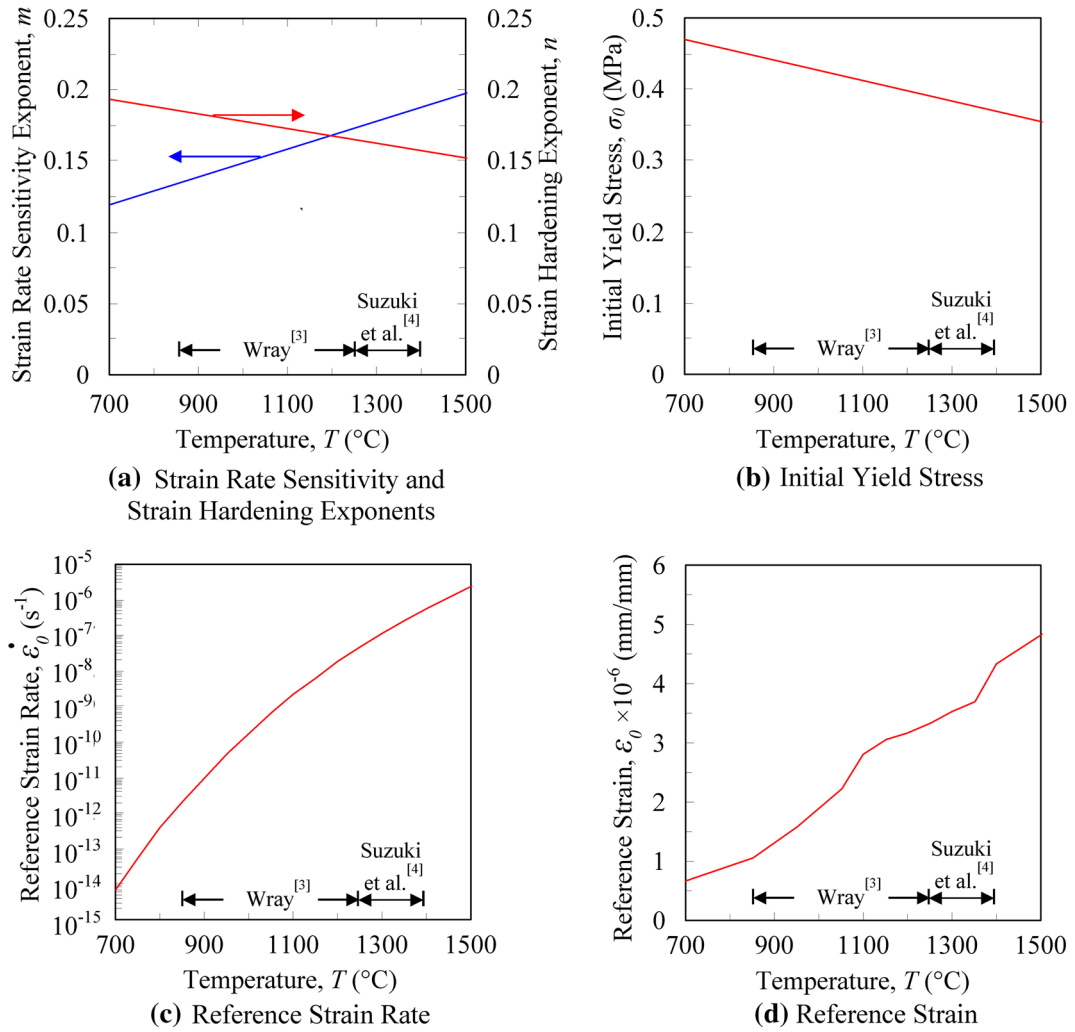


Fig. 6—The strain rate and strain hardening exponents (a), initial yield stress (b), reference strain rate (c), and reference strain (d) as functions of temperature. Parameters were estimated from the experimental data of Wray^[3] [1123 K (850 °C) ≤ T ≤ 1523 K (1250 °C)] and Suzuki *et al.*^[4] [1523 K (1250 °C) ≤ T ≤ 1673 K (1400 °C)].

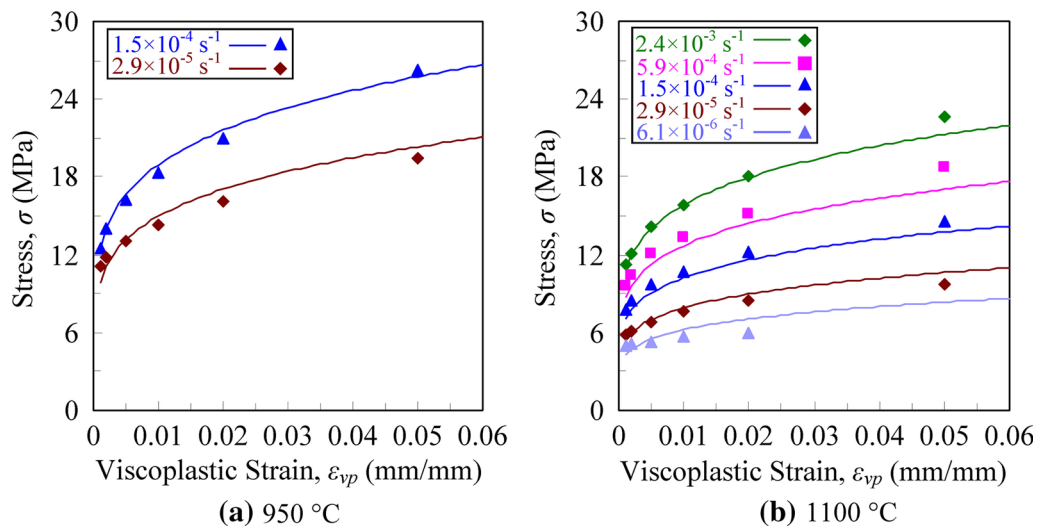


Fig. 7—Comparison between measured (from Wray^[3]) and predicted stresses plotted at several strain rates as a function of viscoplastic strain at 1223 K (950 °C) (a) and 1373 K (1100 °C) (b).

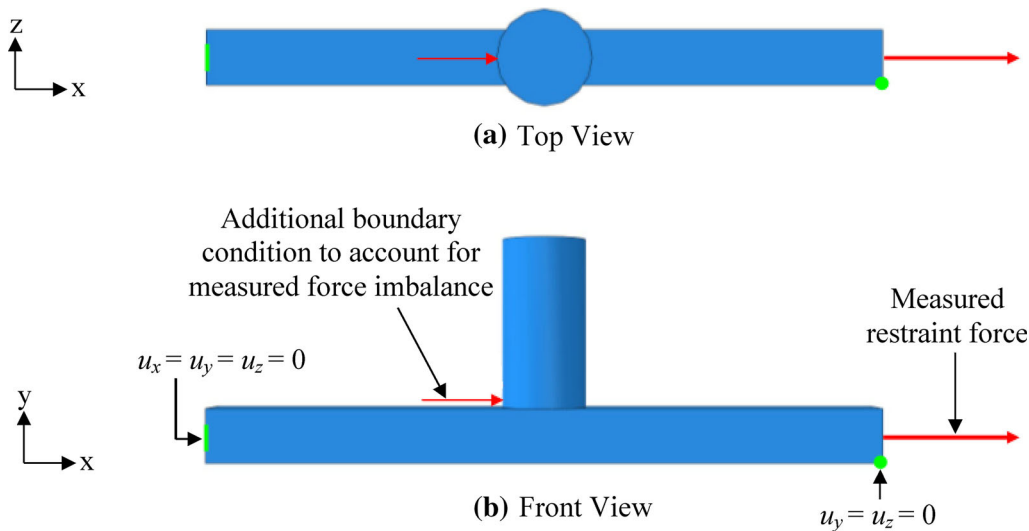


Fig. 8—Top (a) and front (b) views of the ABAQUS® model for the strained bar. An additional force boundary condition was applied at the base of the sprue to account for the measured force imbalance [shown in Fig. 3(c)].

length change for the bar to the axial direction (*i.e.*, $u_y = u_z = 0$). Omission of the force boundary conditions in Figure 8 reduces the model for the strained bars to the unrestrained case.

Through a two-step process, casting distortions were predicted. First, the unrestrained bar experiments were simulated to validate the thermal strain predictions and (if necessary) adjust the thermal expansion coefficient of the steel. Following that, distortions were predicted for the strained bar experiments; any disagreement between measured and predicted axial length changes was eliminated through adjustments to the viscoplastic parameters.

B. Unrestrained Bar Simulations

Length changes for the unrestrained bars owed to thermal strains only. The sole parameters contributing to the thermal strains are the total linear thermal expansion coefficient, α_{tot} , and the temperature for the onset of thermal contraction, T_{th} (see Eq. [9]). For the initial simulation, α_{tot} was determined from IDS using Eq. [10], whereas T_{th} was set to the measured solidus temperature [1683 K (1410 °C)]. The resulting predicted axial length change (blue curves) for unrestrained bar 1 is plotted as a function of time and compared to the measured data (black curves) in Figure 9. The measured solidus temperature at the sprue location (see Figure 1) is denoted by the black vertical dashed line in Figure 9(c). One difference between the curves can be seen during the initial 10 s (see Figure 9(c)), before any substantial solidification of the steel occurs. The measured axial length decreases during the initial 10 seconds, whereas the predicted axial length remains nearly constant during this period. The measured rapid contraction during the initial 10 seconds can be attributed to expansion of the sand mold into the steel. This mold expansion accounts for a 0.15-mm decrease in the length of the bar. Since the mold was not included in the simulation, the effect of mold expansion

could not be predicted. For this reason, the curves for the predicted length change in Figure 9 are shifted downward by 0.15 mm. After 10 seconds, there are still several areas of disagreement between the measured and predicted length changes when using the thermal expansion coefficient from IDS and the solidus temperature for the onset of contractions. The minor discrepancies between 10 and 50 seconds can likely be attributed to small inaccuracies in the predicted temperature fields at early times, immediately after pouring. More importantly, during the remainder of the cooling period, the predicted contraction rate for the bar consistently exceeds the measured rate. This leads to an over-prediction of about 0.5 mm in the axial length change at 12000 seconds, when the bar is near room temperature (see Figure 9(a)).

To better match the measured and predicted contraction curves, modifications to both α_{tot} and T_{th} were required. First, the total linear thermal expansion coefficient was adjusted as shown in Figure 9(d); the entire curve was shifted downward in order to decrease the rate of contraction in the simulation. Also, the magnitude of the step at 948 K (675 °C) (representing the decomposition of austenite to pearlite and α -ferrite) was slightly increased to predict additional expansion during the solid-state phase transformation. These adjustments resulted in the measured and predicted axial length change curves to be exactly parallel during the entire cooling period. To eliminate the remaining shift between the two curves, the temperature for the onset of thermal contractions was increased to $T_{\text{th}} = 1703$ K (1430 °C). This temperature corresponds to a solid fraction of $g_s = 0.98$, as opposed to $g_s = 1$ for the initial simulation. Using the adjusted α_{tot} and T_{th} , excellent agreement between the measured (black curves) and predicted (pink curves) axial length changes can be observed in Figure 9 at all times.

The procedure used to adjust the temperature for the onset of thermal contractions, T_{th} , is illustrated in more detail in Figure 10. The figure compares the measured

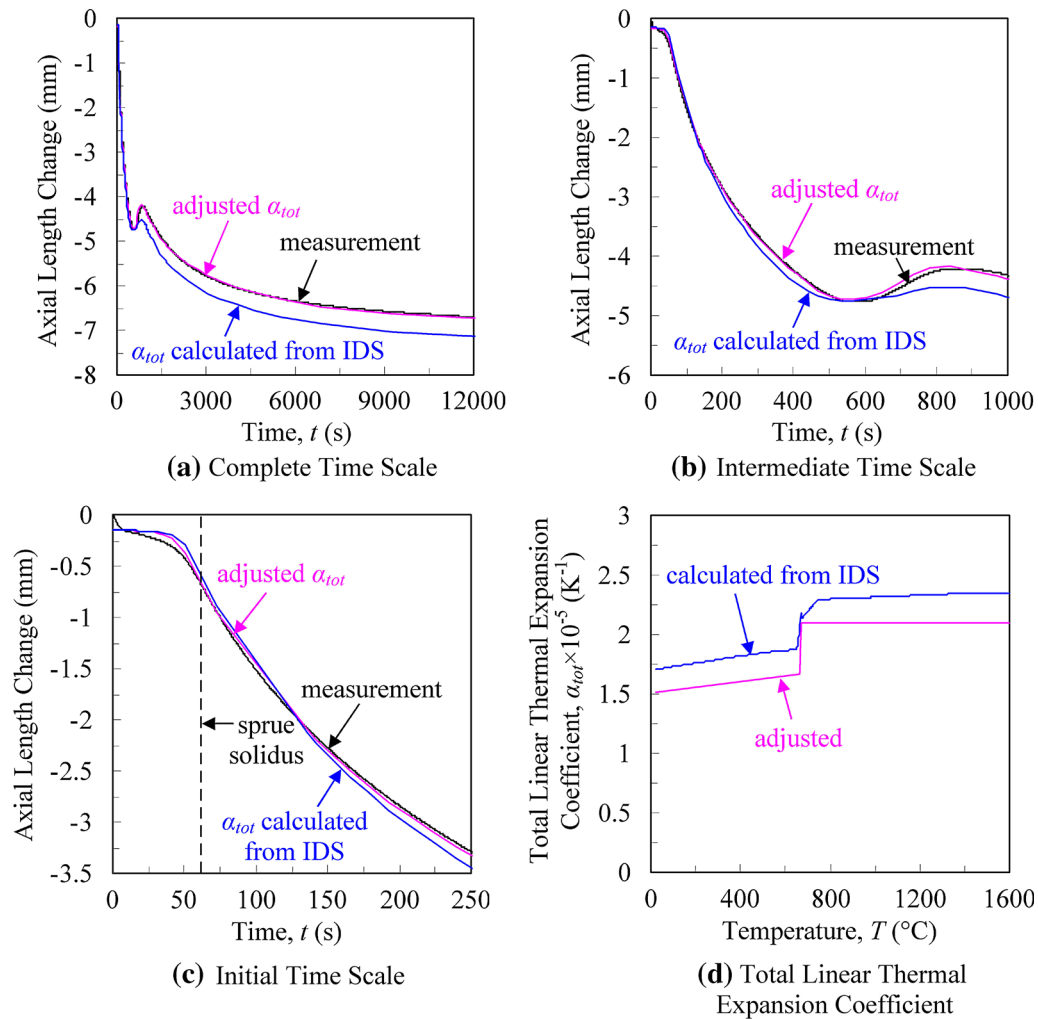


Fig. 9—Measured and predicted axial length changes for the unrestrained bar 1 experiment plotted on complete (a), intermediate (b), and initial (c) time scales. (d) The total linear thermal expansion coefficient was modified as shown.

axial length change during the first 250 s with predictions for three different T_{th} : 1683 K (1410 $^{\circ}C$) ($g_s = 1$), 1703 K (1430 $^{\circ}C$) ($g_s = 0.98$), and 1723 K (1450 $^{\circ}C$) ($g_s = 0.94$). After the first 50 seconds, the curves are parallel to each other, but only the $g_s = 0.98$ curve matches the measurements. At such high solid fractions, only isolated pools of liquid remain within the coherent solid network; hence, it is realistic for thermal contraction to commence before complete solidification. This finding is similar to what Stangeland *et al.*^[37] observed for an aluminum alloy.

For all remaining simulations (unrestrained and strained), the thermal strains were calculated using the adjusted α_{tot} in Figure 9(d). However, because the measured solidus temperature varied [from 1648 K to 1688 K (1375 $^{\circ}C$ to 1415 $^{\circ}C$)] among the experiments (due to differences in the steel chemistries), a different T_{th} was used in each simulation. Using the same procedure as illustrated in Figure 10, the corresponding solid fractions for the onset of thermal contractions varied between 0.95 and 0.98. This variation can be attributed to uncertainties in determining the solidus temperature.

C. Strained Bar Simulations

An example of the accumulated viscoplastic strains predicted by the stress simulation (for strained bar 1) is shown in Figure 11. Due to the hotspot that is created by the sprue near the middle of the bar, the majority of the viscoplastic strain may be expected to occur at that location, since steel yields more easily at higher temperatures. However, the simulation results in Figure 11 indicate that the bar's axial distortions are distributed relatively evenly throughout its entire length. The spot of high strains predicted near each end of the bar is due to the cast steel contracting around the embedded restraining rod and nut. Figure 11 also indicates that the application of the additional force boundary condition at the base of the sprue results in the predicted axial length changes to be slightly larger on the left side of the sprue than on the right side. For the case shown in Figure 11, additional stress simulations were performed in which g_s^{coh} and g_s^{coal} were varied. Due to space limitations, the results are not shown here. It was found that, as expected, the present predictions are insensitive to changes in both g_s^{coh} and g_s^{coal} .

The measured and predicted axial length changes for the strained bar 1 experiment are compared in Figure 12. Initial predictions, labeled as “estimated m ” (pink lines), were obtained using the viscoplastic constitutive model parameters determined from tests with reheated specimens, as explained in Section IV–B. When viewed on the complete time scale (Figure 12(a)), the agreement of the initial predictions with the measurements appears to be good. However, Figure 12(c) shows that during the straining period an excessive amount of viscoplastic strain is predicted. The predicted length increase due to the straining is about 0.8 mm, whereas the measured one is only 0.25 mm. In order to reduce this disagreement, a trial-and-error process was performed in which the strain rate sensitivity exponent, m , was adjusted until the measured and predicted length changes agreed at all times. The final adjusted m curve is shown in Figure 12(d) and compared to the initial estimate. As can be seen from Figures 12(a) through (c), the adjustment produced excellent agreement between the measured and predicted axial length changes for this experiment, especially during the straining period.

The strain rate sensitivity exponent in Figure 12(d) was adjusted from 973 K to 1773 K (700 °C to 1500 °C). However, because distortions were induced mainly at higher temperatures (see Figure 5), the

predicted distortions should be insensitive to variations in m at lower temperatures. Through a parametric study, the predicted distortions were found to be sensitive to changes in m for strained bar 1 from 1298 K (1025 °C) $\leq T \leq$ 1673 K (1400 °C). This range, termed the “calibrated range,” contains the temperatures for which the computational model has been calibrated from the experimental measurements and is included in Figure 12(d). Similar ranges were determined for all other strained bar experiments.

The adjusted m curve in Figure 12(d) is characterized by two segments and a transition region. The first segment [973 K (700 °C) $\leq T \leq$ 1473 K (1200 °C)] was shifted downward from the estimated curve, while the second segment [1633 K (1360 °C) $\leq T \leq$ 1773 K (1500 °C)] was shifted upward. The transition region [1473 K (1200 °C) $< T <$ 1633 K (1360 °C)] connects the two segments to form a piecewise continuous linear curve. Although the discontinuities between subdomains [located at 1473 K and 1633 K (1200 °C and 1360 °C)] are likely unphysical (*i.e.*, a smooth continuous curve should be expected), additional experimental data would be needed to fine-tune the curves and eliminate the kinks. Interestingly, the temperature span of the first segment corresponds to that of the Wray^[3] measurements [1123 K (850 °C) $\leq T \leq$ 1523 K (1250 °C)], while the second segment roughly coincides with the Suzuki *et al.*^[4] temperature range [1523 K (1250 °C) $\leq T \leq$ 1673 K (1400 °C)]. These similarities suggest that parameter estimation from the Wray^[3] measurements leads to an over-prediction of casting stresses, whereas using the Suzuki *et al.*^[4] measurements leads to an under-prediction. To show this apparent correlation, the temperature ranges for the Wray^[3] and Suzuki *et al.*^[4] measurements are included in Figure 12(d) and all subsequent m curve plots.

Choosing which parameter to adjust in the dynamic yield equation, Eq. [16], was determined through a process of elimination. The estimated strain hardening exponent, n , (Figure 6(a)) and initial yield stress, σ_0 , (Figure 6(b)) both decrease with increasing temperature. However, these parameters would need to be increasing functions of temperature above 1633 K (1360 °C) to achieve agreement between the measured and predicted length changes. Such changes would imply that the strength and hardening increase with temperature, both

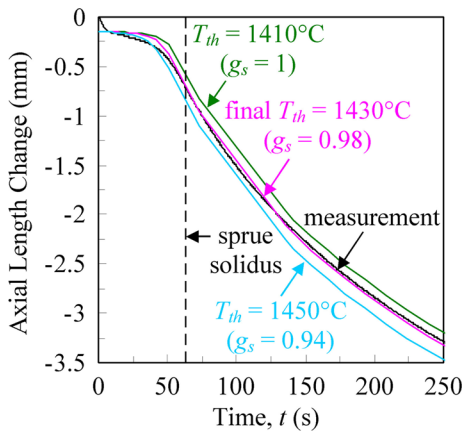


Fig. 10—Parametric study showing the sensitivity of the predicted axial length change (from unrestrained bar 1) to changes in temperature at the onset of thermal contraction, T_{th} .

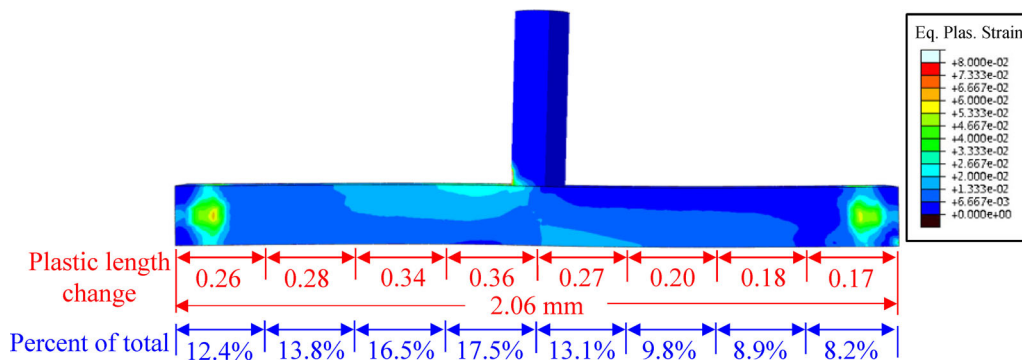


Fig. 11—Total accumulated viscoplastic strains predicted for the strained bar 1 experiment.

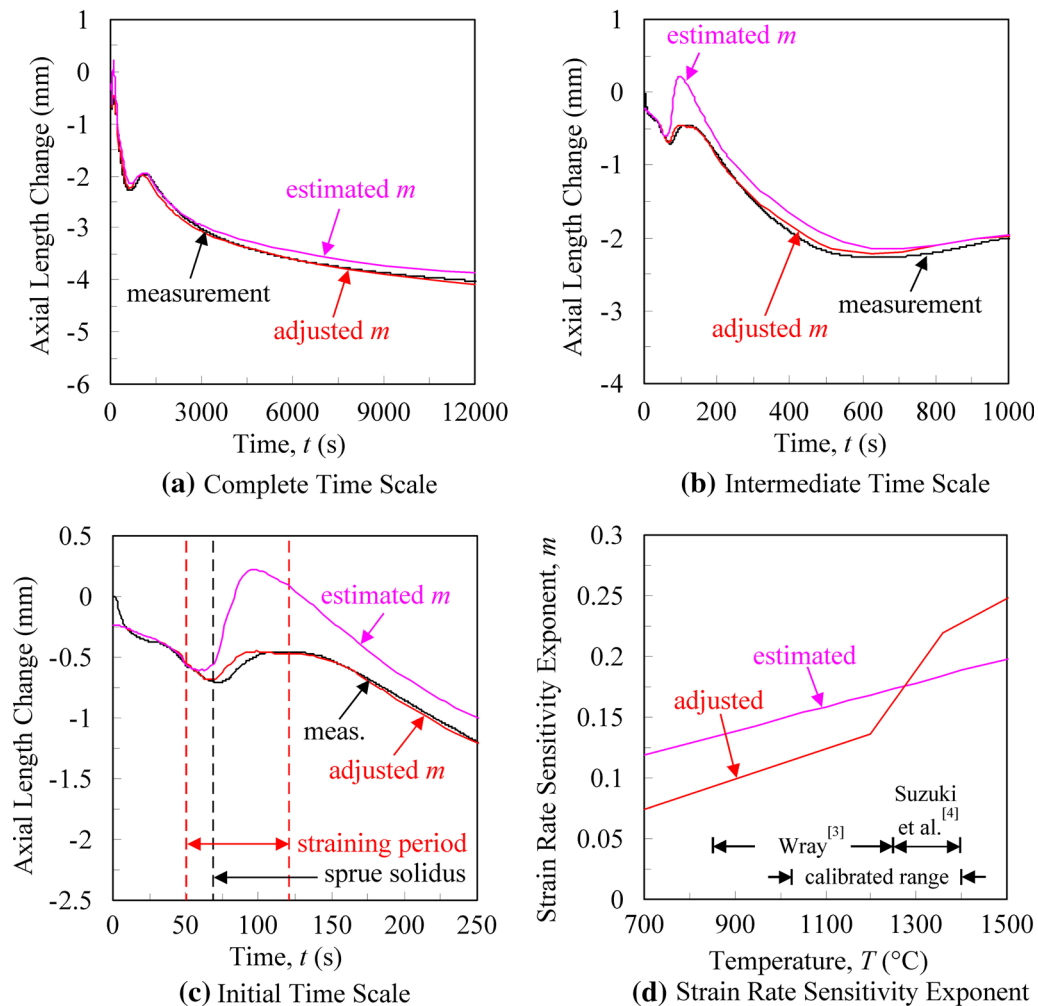


Fig. 12—Measured and predicted axial length changes for the strained bar 1 experiment plotted on complete (a), intermediate (b), and initial (c) time scales. Predicted distortions were sensitive to changes in the strain rate sensitivity exponent (d) only within the calibrated range.

of which are unexpected. Therefore, σ_0 , n , and the reference strain, ϵ_0 , (which is calculated from σ_0 and n) were not modified. Another possibility was to modify the reference strain rate, $\dot{\epsilon}_0$, through adjustments to either the Arrhenius prefactor, A , or the activation energy, Q . However, because A only depends on carbon content (which did not vary significantly among the experiments), only small variations in this parameter would be expected. Also, Q would have to be adjusted as an increasing function of temperature, which is unphysical. This leaves the strain rate sensitivity exponent, m . Strain rate impacts stresses and distortions in steels mainly at high temperatures. This implies that m should increase with temperature, which is indeed the case for both the estimated (Figure 6(a)) and adjusted (Figure 12(d)) strain rate sensitivity exponents. Therefore, m was chosen as the adjustable parameter.

Another example of matching measured and predicted length changes is shown for the strained bar 5 experiment in Figure 13. Here, the length change during the straining period is vastly under-predicted when using the initial estimated m variation from the reheated specimens. This results in the predicted final length of

the bar near room temperature to be about 1.5 mm shorter than what was measured. Adjusting the strain rate sensitivity exponent m in the simulation as shown in Figure 13(d), however, results in excellent agreement in the length changes at all times during the experiment. Note that the adjustments made to m in Figure 13(d) are similar in nature to the ones for the strained bar 1 experiment in Figure 12(d). This similarity is unexpected, because the straining in the two experiments (strained bar 1 and 5) was performed quite differently. Comparing the measured axial length changes in Figures 12(c) and 13(c), it can be seen that bar 1 was strained when it had contracted (freely) by about 0.5 mm, whereas bar 5 was strained much later when it had contracted already by 1.3 mm. Hence, strained bar 1 experienced the majority of the viscoplastic strains at higher temperatures than strained bar 5. As expected, the calibrated range for strained bar 5 [1223 K (950 °C) $\leq T \leq$ 1623 K (1350 °C)] was lower than that for strained bar 1 [1298 K (1025 °C) $\leq T \leq$ 1673 K (1400 °C)]. In order to achieve agreement in the measured and predicted length changes for both experiments, the strain rate sensitivity exponent m had to be

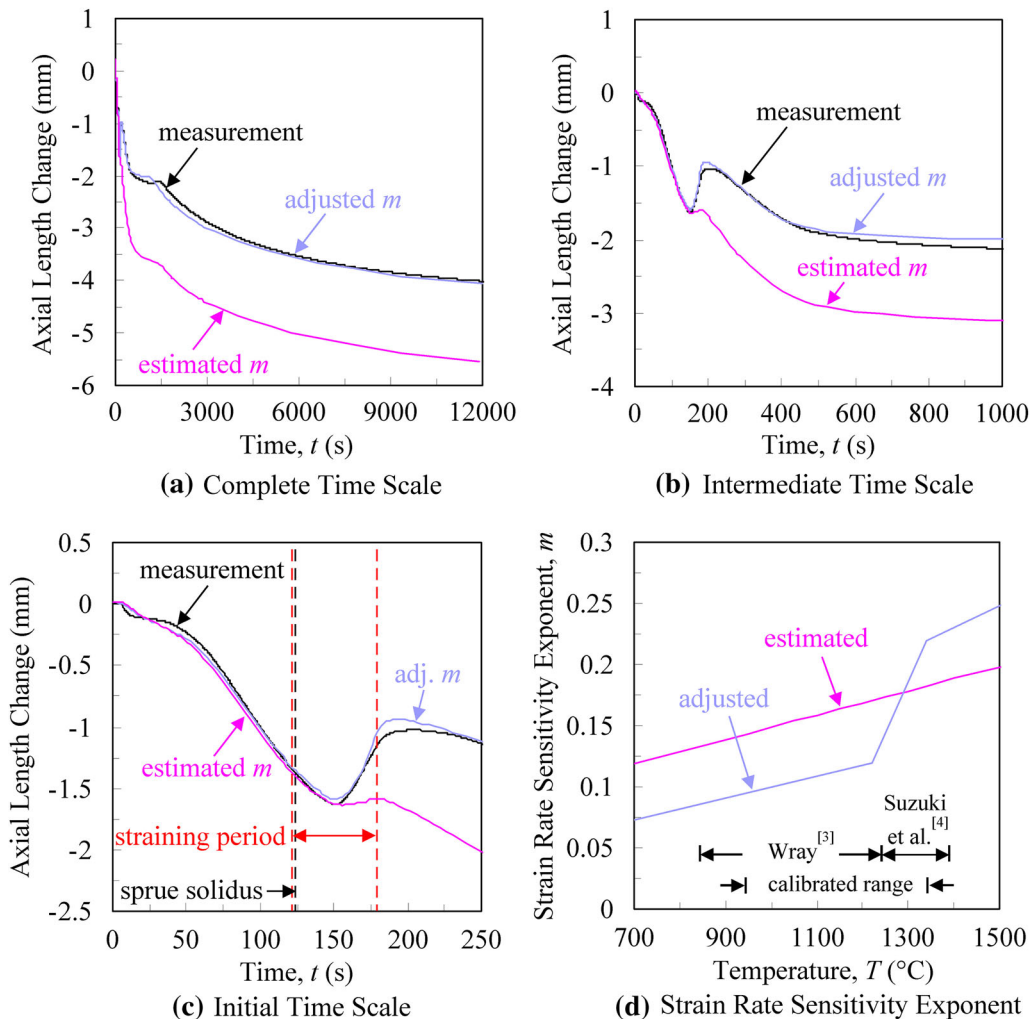


Fig. 13—Measured and predicted axial length changes for the strained bar 5 experiment plotted on complete (a), intermediate (b), and initial (c) time scales. Predicted distortions were sensitive to changes in the strain rate sensitivity exponent (d) only within the calibrated range.

increased at higher temperatures [above 1573 K (1300 °C)] and decreased at lower temperatures [below 1473 K (1200 °C)]. Simply shifting the m curve up or down does not produce good agreement for both experiments.

To further demonstrate the necessity for the adjustments to the strain rate sensitivity exponent, a parametric study was performed for the strained bar 2 experiment, as shown in Figure 14. In this figure, predicted results are shown for the initial simulation (using the initially estimated m curve) and for the final simulation using an adjusted m curve. Again, the initial m curve produces poor agreement and the adjusted m curve achieves excellent agreement between the measured and predicted axial length changes for this experiment. Furthermore, the adjustments made to m (Figure 14(d)) are similar in nature to the ones for the strained bar 1 and 5 experiments (see above). The calibrated range for strained bar 2 spans from 1273 K to 1648 K (1000 °C to 1375 °C), which falls between the bar 1 and 5 ranges. Figure 14 also shows simulation results for two additional simulations (termed “iteration 1” and “iteration 2”) where different m curves were

tried. For the first iteration, the strain rate sensitivity exponent was only adjusted at high temperatures (*i.e.*, the Suzuki *et al.*^[4] range) and the initially estimated values were used at lower temperatures (*i.e.*, the Wray^[3] range), as shown in Figure 14(d). In this iteration, Figure 14(c) indicates that insufficient distortions are predicted during the straining period. For the second iteration, the strain rate sensitivity exponent was matched to the final adjusted curve at lower temperatures, but the initially estimated m curve was used in the high temperature range. As a result, excessive distortions are predicted during the straining period. This clearly demonstrates that adjustments to the strain rate sensitivity exponent at both low and high temperatures (*i.e.*, both the Wray^[4] and Suzuki *et al.*^[4] temperature ranges) are needed in order to match predicted and measured axial length changes. Based on these adjustments, the measurements of both Wray^[3] and Suzuki *et al.*^[4] appear to be inadequate for determining the mechanical behavior of steel during casting.

Figure 15(a) shows that excellent agreement was achieved between measured and predicted axial length changes for all five strained bar experiments. This

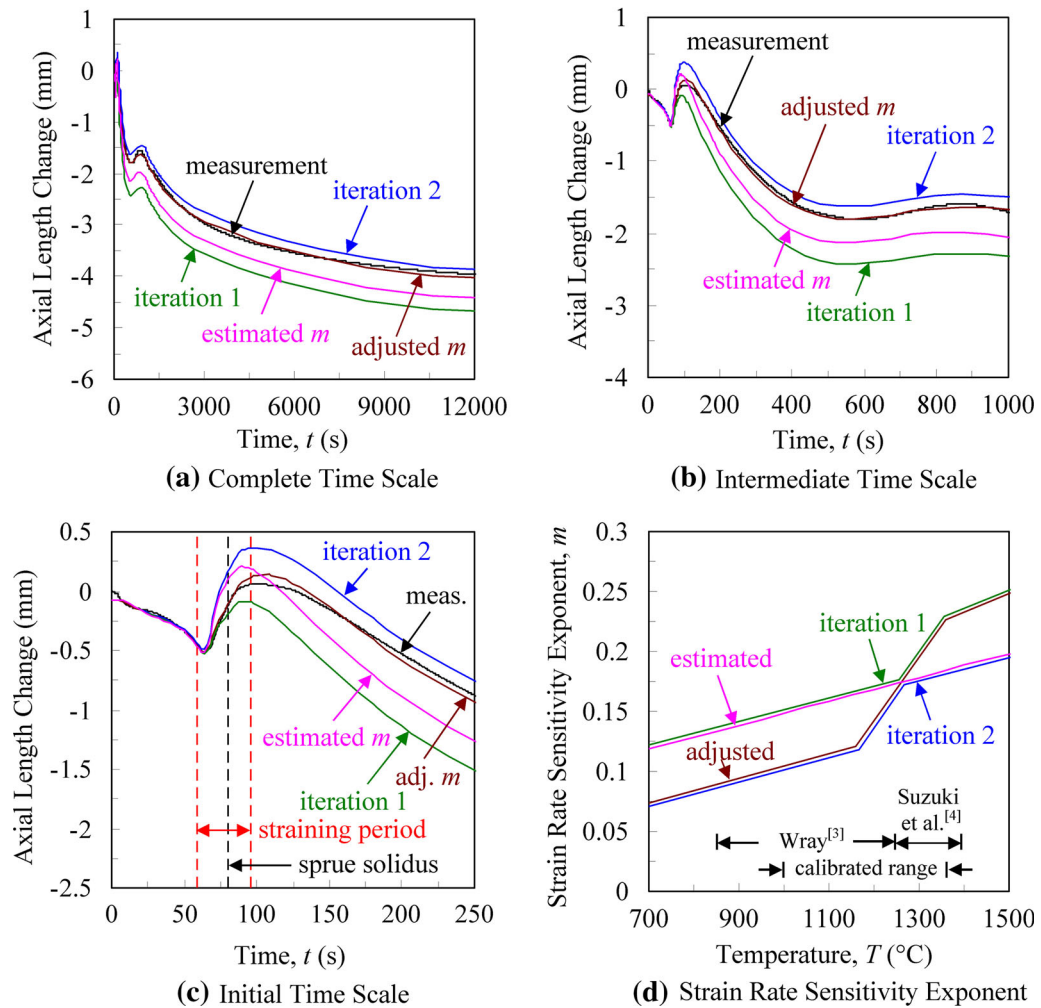


Fig. 14—Predicted axial length change for the strained bar 2 experiment plotted on complete (a), intermediate (b), and initial (c) time scales. Predicted distortions were sensitive to changes in the strain rate sensitivity exponent (d) only within the calibrated range. Two additional stress simulations (iterations 1 and 2) demonstrated the need to adjust m in both the Wray^[3] and Suzuki *et al.*^[4] temperature ranges.

figure is limited to the first 250 seconds, because afterwards the strains are predominately thermal and the axial length change curves are almost parallel. The axial length changes are different in each experiment because of variations in the straining period (beginning and duration), the sprue diameter (for strained bar 5), and the steel composition. Hence, each of the 5 experiments provides independent data with which the strain rate sensitivity exponent could be calibrated. The final adjusted strain rate sensitivity exponent curves are compared for all experiments in Figure 15(b). They all show the same behavior, and a single “representative” m curve can be constructed (thick black line in Figure 15(b)) that produces good agreement between measured and predicted axial length changes in all experiments. The piecewise expression for this curve is provided in Table III. In addition, the total calibrated range in Figure 15(b) combines the calibration ranges from all strained bar experiments and represents the temperatures for which the computational model has been calibrated for the present study.

The difference between the estimated and adjusted strain rate sensitivity exponent curves in Figure 15(b) represents the major finding of this study. The adjusted m curve, together with the other parameters in Figure 6, comprises the set of viscoplastic parameters needed to model the mechanical behavior of austenite during casting. To illustrate the differences between constitutive datasets using the estimated and adjusted m , representative stress–strain curves [at 1273 K, 1473 K, and 1673 K (1000 °C, 1200 °C, and 1400 °C) for a 0.25 pct C steel and 1.5×10^{-5} 1/s strain rate] were generated and are shown in Figure 16. At 1273 K and 1473 K (1000 °C and 1200 °C), the predicted stresses using the estimated m are considerably higher [48 pct at 1273 K (1000 °C) and 28 pct at 1473 K (1200 °C)] than those using the adjusted m . At 1673 K (1400 °C), the opposite is true; the predicted stresses are higher by 13 pct when using the adjusted m . These significant differences demonstrate that estimating mechanical constitutive parameters using reheated steel specimens may not be appropriate for stress simulations of casting processes.

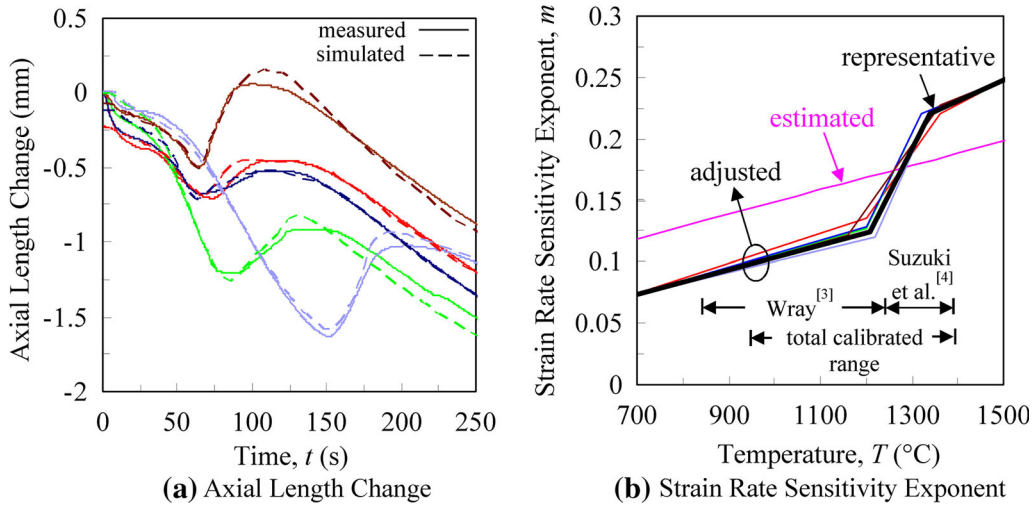


Fig. 15—Measured and simulated axial length changes for all strained bar experiments shown in (a). The estimated, adjusted, and representative strain rate sensitivity exponents are summarized in (b). The total calibrated range [1223 K (950 °C) ≤ T ≤ 1673 K (1400 °C)] represents the temperature range over which the computational model has been calibrated for the present study.

Table III. Expression for Representative Strain Rate Sensitivity Exponent from Fig. 15(b)

Strain Rate Sensitivity Exponent	Temperature, T [K (°C)]
$6.373 \times 10^{-3} + 9.804 \times 10^{-5} T$	973 (700) ≤ T ≤ 1483 (1210)
$-7.592 \times 10^{-1} + 7.308 \times 10^{-4} T$	1483 (1210) < T ≤ 1633 (1360)
$-3.125 \times 10^{-2} + 1.875 \times 10^{-4} T$	T > 1633 (1360)

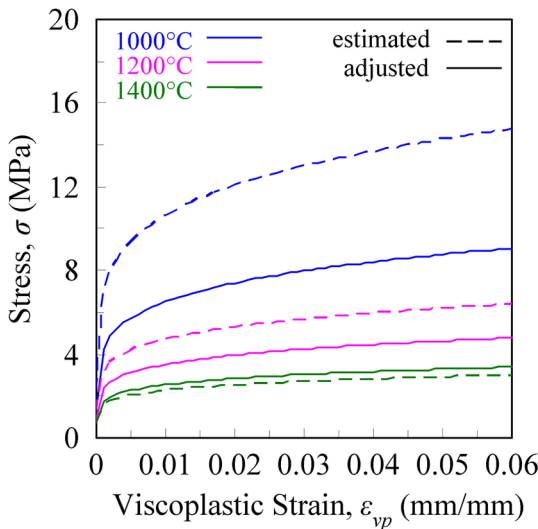


Fig. 16—Comparison between predicted stresses for constitutive datasets using estimated and adjusted strain rate sensitivity exponents for a 0.25 pct carbon content and 1.0×10^{-5} 1/s strain rate.

They also show the importance of calibrating the constitutive model using *in situ* measurements.

VI. CONCLUSIONS

In this study, forces and displacements were measured *in situ* during casting of a steel bar in a sand mold. Using

embedded bolts at the two ends, the bar was strained during solidification and cooling to induce stresses and distortions. Multiple experiments with different straining periods were conducted. The experiments were simulated using a finite element stress analysis code employing an elasto-visco-plastic constitutive law that accounts for solidification. The thermal strain predictions were calibrated first using displacement measurements from the unrestrained bar experiments. The simulations for the strained bar experiments used the measured forces in the bolts as boundary conditions. It was shown that using constitutive model parameters determined from previous mechanical tests involving reheated steel specimens does not produce satisfactory agreement between the measured and predicted length changes for the strained bar experiments. This disagreement sheds considerable doubt on previous stress simulations of steel casting processes. Through a trial-and-error process involving repeated simulations of the experiments, the temperature dependence of the strain rate sensitivity exponent was adjusted until good agreement between the measured and predicted length changes was obtained. The adjustments were shown to be essentially the same for all experiments, even though the straining periods were different in each of the experiments. The significance of the adjustments in the viscoplastic parameter was demonstrated through a parametric study.

The present study has resulted in a validated mechanical property dataset from 1223 K to 1673 K (950 °C to 1400 °C) for the austenite phase of steel during casting. The data reveal a significantly different mechanical

behavior of steel during casting compared to what previous stress–strain data from reheated specimens show. This discrepancy may be attributed to differences in the microstructure. It is envisioned that the present study leads to more accurate stress simulations of steel casting processes. Additional work is needed to cover a wider range of steel compositions, other steel phases (e.g., ferrite), and temperatures below 1223 K (950 °C).

ACKNOWLEDGMENTS

This research was sponsored through the Defense Logistics Agency through the American Metal Consortium and the Steel Founders' Society of America.

REFERENCES

1. P. Feltham: *Phys. Soc. Proc.*, 1953, vol. 66 (406B), pp. 865–83.
2. P.J. Wray and M.F. Holmes: *Metall. Mater. Trans. A*, 1975, vol. 6A (6), pp. 1189–96.
3. P.J. Wray: *Metall. Mater. Trans. A*, 1982, vol. 13A, pp. 125–34.
4. T. Suzuki, K.H. Tacke, K. Wunnenberg, and K. Schwerdtfeger: *Ironmak. Steelmak.*, 1988, vol. 15 (2), pp. 90–100.
5. L. Anand: *J. Eng. Mater. Technol.*, 1982, vol. 104 (1), pp. 12–17.
6. P.F. Kozlowski, B.G. Thomas, J.A. Azzi, and H. Wang: *Metall. Mater. Trans. A*, 1992, vol. 23A, pp. 903–18.
7. C. Li and B.G. Thomas: *Metall. Mater. Trans. B*, 2004, vol. 35B, pp. 1151–72.
8. S. Koric and B.G. Thomas: *Int. J. Numer. Methods Eng.*, 2006, vol. 66, pp. 1955–89.
9. S. Koric and B.G. Thomas: *2007 Abaqus Users Conference*, Paris, 2007.
10. S. Koric and B.G. Thomas: *J. Mater. Process. Technol.*, 2008, vol. 197, pp. 408–18.
11. S. Koric and B.G. Thomas: *Int. J. Numer. Methods Eng.*, 2009, vol. 78, pp. 1–31.
12. J. Sengupta, C. Ojeda, and B.G. Thomas: *Int. J. Cast Met. Res.*, 2009, vol. 22 (1–4), pp. 8–14.
13. A.E. Huespe, A. Cardona, N. Nigro, and V. Fachinotti: *J. Mater. Process. Technol.*, 2000, vol. 102, pp. 143–52.
14. A.E. Huespe, A. Cardona, and V. Fachinotti: *Comput. Methods Appl. Mech. Eng.*, 2000, vol. 182, pp. 439–55.
15. C. Zhang, M. Bellet, M. Bobadilla, H. Shen, and B. Liu: *Metall. Mater. Trans. A*, 2010, vol. 41A, pp. 2304–17.
16. R.N. Parkins and A. Cowan: *Proceedings of the Institute of British Foundation*, Paper No. 1062, 1953, p. A101-9.
17. C. Monroe and C. Beckermann: *61st Steel Founders Society of America Technical and Operating Conference*, Paper No. 5.7, Steel Founders' Society of America, Chicago, IL, 2006.
18. P. Ackermann, J.D. Wagniere, and W. Kurz: *Mater. Sci. Eng.*, 1985, vol. 75, pp. 79–86.
19. M. Rowan, B.G. Thomas, R. Pierer, and C. Bernhard: *Metall. Mater. Trans. B*, 2011, vol. 42B, pp. 837–51.
20. MAGMASOFT® v4.6, Magma GmbH, Aachen.
21. J. Miettinen: *Metall. Mater. Trans. B*, 1997, vol. 28B (2), pp. 281–97.
22. D. Galles and C. Beckermann: *66th Steel Founders Society of America Technical and Operating Conference*, Paper No. 5.2, Steel Founders' Society of America, Chicago, IL, 2012.
23. K.D. Carlson and C. Beckermann: *Int. J. Cast Met. Res.*, 2012, vol. 25, pp. 75–92.
24. C. Monroe: Ph.D. Thesis, University of Iowa, Iowa City, IA, 2009.
25. M. Pokorny, C. Monroe, and C. Beckermann: *Int. J. Metalcast.*, 2008, vol. 2 (4), pp. 41–53.
26. J. Bluhm and R. DeBoer: *ZAMM: J. Appl. Math. Mech.*, 1997, vol. 77 (8), pp. 563–77.
27. A.P. Roberts and E.J. Garboczi: *J. Am. Ceram. Soc.*, 2000, vol. 83 (12), pp. 3041–48.
28. R.A. Hardin and C. Beckermann: *Metall. Mater. Trans. A*, 2007, vol. 38A, pp. 2992–3006.
29. ABAQUS®, Abaqus, Inc., Providence, RI.
30. J.C. Simo and T.J.R. Hughes: *Computational Inelasticity*, Springer-Verlag New York Inc., New York, NY, 1998.
31. C. Martin, M. Braccini, and M. Suery: *Int. J. Plast.*, 2002, vol. 15, pp. 981–1008.
32. A.C.F. Cocks: *J. Mech. Phys. Solids*, 1989, vol. 37 (6), pp. 693–715.
33. V. Tvergaard and A. Needleman: *Acta Metall.*, 1984, vol. 23 (1), pp. 157–69.
34. E.B. Marin and D.L. McDowell: *Comput. Struct.*, 1997, vol. 63 (3), pp. 579–600.
35. B.G. Thomas: *ISIJ Int.*, 1995, vol. 35 (6), pp. 737–43.
36. C.A. Monroe, C. Beckermann, and J. Klinkhammer: *Modelling of Casting, Welding, and Advanced Solidification Processes XII*, S.L. Cockcroft and D.M. Maijer, Wiley, Warrendale, PA, 2009, pp. 643–49.
37. A. Stangeland, A. Mo, O. Nielsen, D. Eskin, and M. M'Hamdi: *Metall. Mater. Trans. A*, 2004, vol. 35A, pp. 2903–15.